Pergamon

PII: S0045-7949(97)00103-X

Computers & Structures Vol. 66, No. 5, pp. 571–583, 1998

Printed in Great Britain
0045-7949/98 $19.00 + 0.00

PENETRATION/PERFORATION OF ALUMINUM, STEEL AND TUNGSTEN PLATES BY CERAMIC RODS

N. V. Nechitailo and **R. C. Batra**†

Department of Engineering Science and Mechanics, Virginia Polytechnic Institute and State University, Blacksburg, VA 24061-0219, U.S.A.

(*Received* 19 *December* 1996; *accepted* 29 *August* 1997)

Abstract—The axisymmetric penetration/perforation of rigidly clamped circular metallic plates by fast moving AD-85 ceramic cylindrical rods has been studied. The ceramic is modeled as an elastic–plastic material with pressure cut-off and the target material is modeled as linearly strain-hardening elastic–plastic material with a material point failing when the effective plastic strain there attains a prescribed value; failed elements are removed from the analysis. For low impact speeds, the ceramic rod fails causing a shallow crater in the metallic target. However, at impact speeds in the range of 1 to 5 km/s, the partially destroyed ceramic rods perforate through the metallic targets. The effect of material parameters of the metallic plates on the efficiency of penetration has been studied. © 1998 Elsevier Science Ltd. All rights reserved

Key words—kinetic energy penetrators, metallic targets, finite element method, multiple impacts, elastic–plastic material, material failure

INTRODUCTION

The dynamic response of engineering ceramics to impulsive loading has been studied during the last thirty years. The commercial AD-85 alumina has been shown to exhibit the following features: the loss of shear strength during shock loading, reduction of the spall strength with an increase in the intensity of the compression shock, multiple microcracking and viscous flow associated with local melting [1, 2]. The residual spall strength after passage of the compressive wave is shown to be a function of the initial impact speed [3]. Furthermore, strength of ceramics is quite high under shock loading [4]. The Hugoniot elastic limit of ceramics (~6–10 GPa) is very high compared with that of high-strength metallic alloys (~1–3 GPa) [1, 5]. Good fracture toughness and high Hugoniot elastic limit of ceramics have been used to protect metallic and composite structures from damage during a penetration event by bonding ceramic layers on their outside surfaces. The high strength and inertia of ceramic layers result in high impact stresses leading to fracture or severe plastic deformations of steel projectiles.

Although there is considerable theoretical and experimental work on the use of ceramics as targets, we have not found any published theoretical or experimental study on using ceramics as penetrators. It could be due to the fact that ceramic projectiles are perceived to be too weak and crushable to penetrate hard steel targets. However, because of their high Hugoniot elastic limit and compressive strength, it seems that they should be able to impart high kinetic energy to the metallic target and deform it severely. An objective of this study is to demonstrate that indeed ceramic rods can perforate even tungsten targets at moderate impact speeds. We use simple material models, assume that an element fails when the effective plastic strain in it reaches a critical value and delete failed elements from the analysis. This approach to deal with failed elements was developed and popularized by Stetcher and Johnson [10] and is currently in wide use, for example, see Refs [11, 12].

FORMULATION OF THE PROBLEM

We use the Lagrangian/referential description of motion to analyze the axisymmetric deformations of a rigidly clamped circular metallic plate impacted at normal incidence by a fast moving cylindrical ceramic rod. Equations expressing the balance of mass and linear momentum may be found in Truesdell and Noll [6]. Even though such impact problems involve high pressures and possibly high temperatures, especially at points adjoining the target–penetrator interface, the dependence of material properties upon the temperature is neglected and a mechanical problem is analyzed herein.

The target material (aluminum, steel or tungsten) is modeled as elastic–plastic with linear strain-hardening. An element is assumed to fail when the effective plastic strain in it reaches a preassigned value

†Author to whom all correspondence should be addressed.

and failed elements are removed from the analysis. The ceramic material is modeled as elastic–plastic with a pressure cut-off. The experimental work of Rosenberg [8] on AD-85 ceramic suggests that the dynamic yield stress, σ_{dyn}, depends affinely upon the hydrostatic pressure p, but is independent of the effective strain-rate; thus

$$\sigma_{dyn} = \sigma_{st} + pA, \tag{1}$$

where σ_{st} equals the yield stress in a uniaxial simple compression test, p is taken to be positive in compression and

$$A = 3[(1-2\nu)\sigma_H - (1-\nu)\sigma_{st}]/[(1+\nu)\sigma_H]. \tag{2}$$

Here ν is Poisson's ratio and σ_H is the Hugoniot elastic limit. We note that values of σ_H and σ_{st}, and hence of A, are different in compression and tension; these are given by:

$$\sigma_H^t = \frac{(1-\nu)}{(1-2\nu)}\sigma_{dyn}, \tag{3}$$

$$\sigma_H^c = \sigma_H^t(\sigma_{st}^c/\sigma_{st}^t), \tag{4}$$

where the superscripts t and c signify tensile and compressive loading, respectively. Following Rajendran [7], we use the modified Mie–Gruneisen equation of state to model the volumetric behavior of the AD-85 ceramic under impact loading. Neglecting thermal effects and assuming that the ratio of the bulk to shear moduli degraded due to the evolution of porosity and/or microcracks is the same as that of the intact material, we obtain:

$$p = \alpha R_k[2 - \Gamma + (-3 + 2.5\Gamma)e^{\epsilon_v} + (1-2\Gamma)e^{2\epsilon_v} + 0.5\Gamma^{3\epsilon_v}],$$

where

$$R_k = 2(1-f)(1-2\nu)/[2(1-2\nu) + f(1+\nu)]. \tag{6}$$

Here, α is the effective bulk modulus and takes account of the degradation of the material properties of the ceramic due to its initial porosity, f is the void fraction or porosity of the material, Γ is the Mie–Gruniesen parameter, R_k the Mackenzie correction factor and $\epsilon_v = \ln(v/v_0)$ is the volumetric strain, where v and v_0 are the present and specific volumes. During elastic unloading from a plastic state, we assume that the bulk modulus stays constant and its magnitude equals α, the slope of the equation of state at $\epsilon_v = 0$. A ceramic material point is assumed to fail when the hydrostatic pressure there is tensile and its magnitude exceeds the spall strength of the material.

At the target–penetrator interface, we impose the condition of impenetrability and assume that the dynamic coefficient of friction, μ, is given by

$$\mu = \mu_k + (\mu_s - \mu_k)e^{-\gamma v_{rel}}, \tag{7}$$

where μ_s and μ_k are the static and kinetic coefficients of friction respectively, γ is a transition coefficient and v_{rel} is the relative speed between the two sliding surfaces. Frictional forces are not anticipated to play any significant role in this problem because of the quick failure of ceramic elements. All bounding surfaces of the penetrator except the target–penetrator interface are traction free. The target plate is assumed to be rigidly clamped at its periphery and other surfaces except the target–penetrator interface are taken to be traction free.

Initially the target particles are at rest and are unstressed and the penetrator particles are moving in the axial direction with a uniform speed V_0. The penetrator strikes the target at normal incidence and the deformations of both the penetrator and the target are assumed to be axisymmetric.

RESULTS AND DISCUSSION

The afore-stated problem is highly nonlinear due to both geometric and material nonlinearities and is difficult to solve analytically. We seek its approximate solution by the finite element method and use the explicit general purpose code DYNA2D [9]. It employs four-noded quadrilateral elements, an explicit time integration scheme, a one-point quadrature rule to evaluate various integrals and an hour-glass control to eliminate spurious modes. We used the standard DYNA2D hour-glass stabilization method with the hour-glass viscosity coefficient = 0.10, bulk viscosity type 1, quadratic bulk viscosity = 1.5 and linear shock viscosity coefficient = 0.06. The time step equalled 20% of that computed in the code from the Courant condition (i.e. the time required for an elastic wave to travel through the smallest element in the mesh). As is evident from the finite element discretization of the penetrator and the target shown in Fig. 1, both the penetrator and the target are divided into uniform rectangular elements. The deforming regions are rezoned after a few elements have failed and/or other elements have been severely distorted; the rezoning option in DYNA2D is employed for this purpose. The 'automatic contact' feature in DYNA2D was used to identify surfaces of potential contact after each time step. The scale factor for automatic slideline penalty parameter was assigned the value 1.2 and $\mu_k = 0.06$, $\mu_s = 0.78$ and $\gamma = 0.0055$.

In order to compute the numerical results presented below, the following values are assigned to various material parameters; the values of geometric parameters are indicated in Fig. 1. AD-85 Ceramic [7, 8]: Poisson's ratio, $\nu = 0.22$; Mie Gruniesen parameter, $\Gamma = 1.0$; initial mass density, $\rho = 3420\ kg/m^3$; shear modulus, $\mu = 108$ GPa; static tensile yield stress, $\sigma_{st}^t = 0.155$ GPa; static compressive yield stress, $\sigma_{st}^c = 1.93$ GPa; spall strength, $\sigma_{sp} = 0.4$ GPa; effective bulk modulus, $\alpha = 186$ GPa; Hugoniot elastic limit in compression, $\sigma_H^c = 6$ GPa.

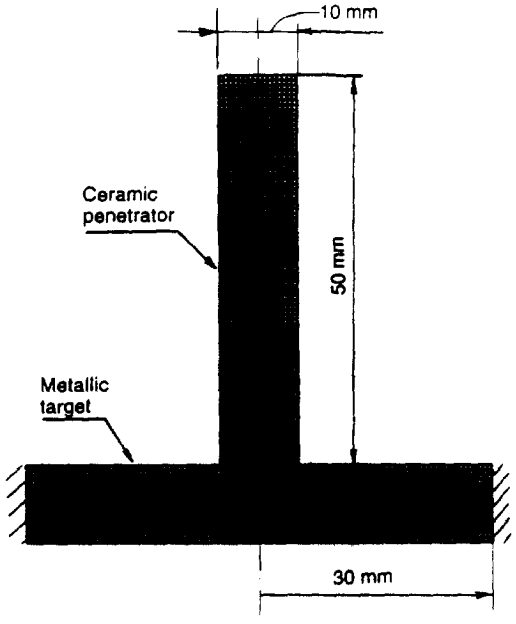

Fig. 1. Schematic sketch of the problem studied and finite element discretization of the penetrator and the target.

For the target materials, the material properties are listed in Table 1.

Upon impact, compressive stress waves are generated in both the penetrator rod and the target plate. For subsonic impacts these waves propagate at the sound speed of the materials and at the shock speed for impacts at hypervelocity. These are followed by slower moving shear waves. The two waves propagate until they interact with a free surface from which a compressive wave is reflected as a tensile wave. For proper duration and amplitude of the tensile pulse, material failure by a variety of mechanisms can occur, see Ref. [5]. Since the penetrator is slender, the interaction between incident and reflected waves in it results in rather complicated and interesting failure patterns. Depending on the target material, geometry and impact conditions, a projectile can lose its nose, or it can break or buckle or different regions can get eroded away. We discuss these below for three different target materials.

Target plate made of 6061-T6 aluminum

Figure 2 depicts the deformed configurations of the ceramic rod and the aluminum plate at three instants of time and for impact speeds of 0.5 and 3 km/s; the failure patterns in the ceramic rod and the aluminum plate in the two cases are quite different. At an impact speed of 0.5 km/s, the central portion of the ceramic rod near the impact surface fails 2 μs after impact making it a hollow cylinder of nonuniform thickness. The hollow cylinder cuts a concave cavity in the plate. At 22 μs, the failed region has propagated along the axis of the penetrator to the rear free end and the central portion of the target plate has been bent. The deformation patterns in the penetrator and the target plate remain essentially unchanged until 41.6 μs and the plate is not perforated in this case. However, for an impact speed of 3 km/s, ceramic material near the impacted end of the penetrator is severely deformed and the penetrator nose becomes conical at 1.6 μs after impact. In addition, there is a crater formed in the aluminum plate. Because of the erosion of the penetrator material, there is a gap between the ceramic rod and the aluminum target; the intact portion of the rod impacts the plate again causing severe damage and essentially a hole in the plate at 8.4 μs. Because of the kinetic energy imparted to the plate, the hole diameter near the back surface of the plate becomes larger with time and the penetrator moves through it.

For impact speeds of 2, 4 and 5 km/s, the sequences of deformations of the penetrator and the target are essentially similar to those observed at an impact speed of 3 km/s. For a 5 km/s impact speed, the flat impacted end of the penetrator is deformed into a conical one at 1.19 μs which because of the failure/erosion of the material becomes flat again at 2.39 μs and impacts the target surface at a subsequent time. At 4.39 μs, there is a large crater formed in the aluminum plate and a significant portion of the ceramic material in the interior of the penetrator has failed. There is a hole formed in the plate at 6 μs and the penetrator passes through it subsequently. Because of the kinetic energy imparted to the plate, the hole diameter continues to grow.

A major difference between the impact of an aluminum plate by a fast moving metallic rod and a ceramic rod is that in the former case, the penetrator nose is generally deformed into a mushroom, the target–penetrator interface moves into the target and multiple impacts do not occur. However, for the ceramic penetrator, a significant portion of the material near the impacted end is

Table 1. Material properties of the target materials

Material parameter	6061-T6 aluminum	4340 steel	D17-tungsten
Young's modulus, E (GPa)	73.3	200.00	350.00
Poisson's ratio, ν	0.28	0.29	0.28
Yield stress, σ_0 (MPa)	298.00	970.00	1550.00
Tangent modulus, E_T (GPa)	0.38	0.47	1.23
Effective plastic strain at failure	0.85	0.77	1.75
Mass density (kg/m^3)	2700.00	7850.00	17000.00

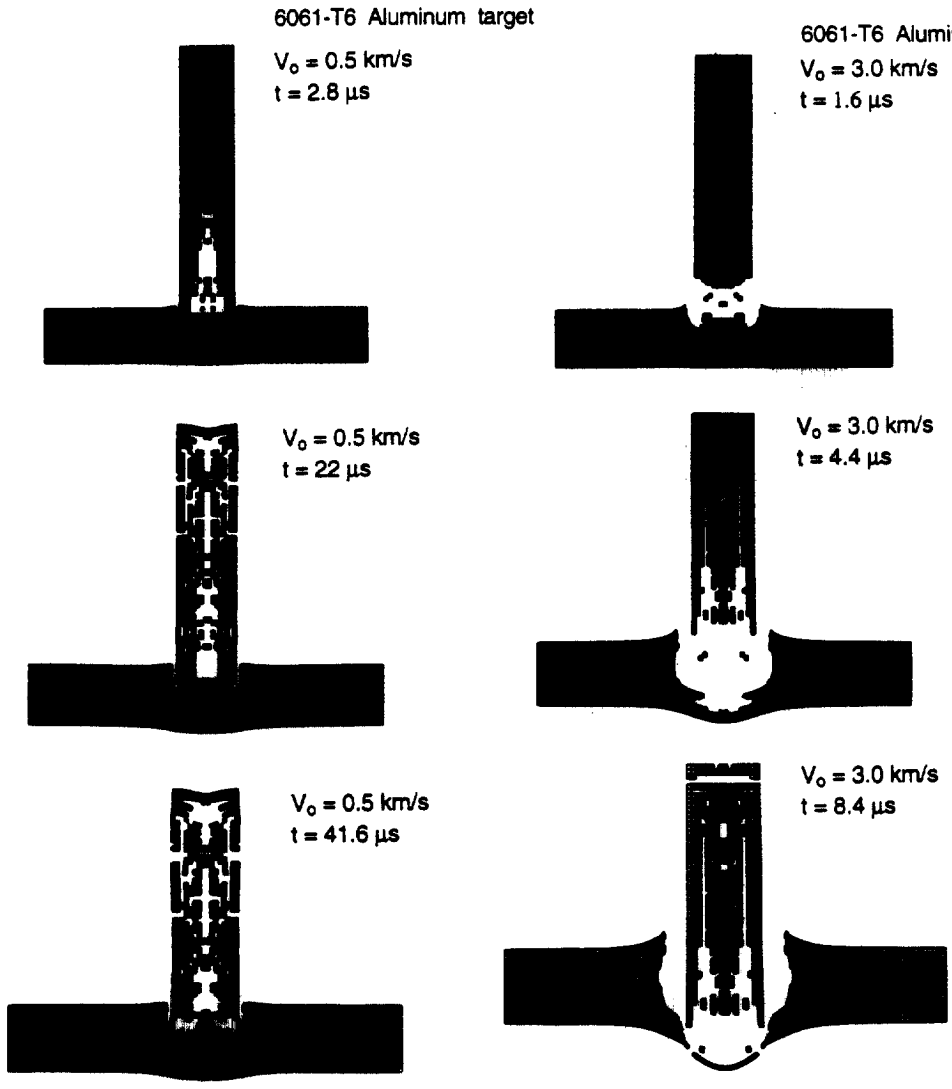

Fig. 2. Deformed configurations of the ceramic penetrator and the aluminum target plate at three instants of time for impact speeds of 0.5 and 3 km/s.

severely deformed and multiple impacts between the moving rod and the target transfer momentum to the deforming crater surface in the target. In both cases, deformations of the penetrator and the target depend strongly upon the impact speed. For a ceramic rod moving at 12 km/s just prior to impact, the complete perforation of the aluminum plate occurred in 2.5 μs and the penetrator nose experienced very little failure. When the target density was artificially increased to 10 times its normal value, we observed multiple impacts at an impact speed of 4 km/s, a parabolic crater during a late stage of penetration and almost complete erosion of the rod. The shape of the crater depends strongly upon the failure strain presumed for the target material. For small values of the failure strain, a smooth cylindrical crater is formed, but for high values of the failure strain, the crater is hemispherical with rough surfaces.

The evolution of the crater depth for different impact speeds is depicted in Fig. 3. These plots indicate that there is no perforation of the aluminum plate at an impact speed of 0.5 km/s and the perforation times for impact speeds of 3, 4, 5 and 6 km/s are considerably smaller than those for an impact speed of 1 km/s. The perforation time does not decrease monotonically as the impact speed is increased from 1 to 6 km/s. This could be due to the differences in the failure of the penetrator near the impacted end, the number of multiple impacts and the shape of the crater formed.

We have deleted failed elements irrespective of their locations. Thus, the kinetic energy associated with these failed elements is removed from the analysis and the space occupied by them just prior to failure is replaced by vacuum. In experiments the failed material may not disappear instantaneously. Thus, some of the computed shapes of the target

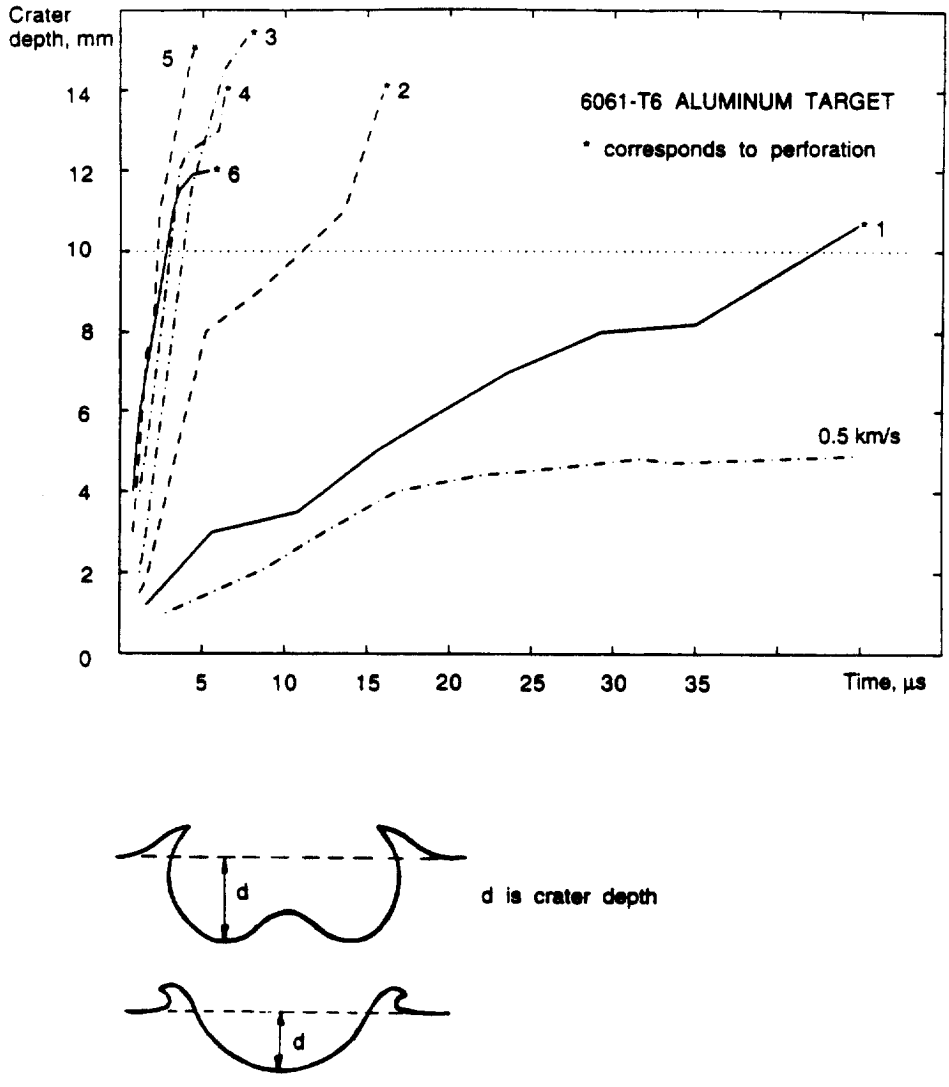

Fig. 3. Time history of the evolution of the crater depths in the aluminum plate struck at normal incidence by a ceramic rod at different impact speeds. The dotted horizontal line corresponds to the initial thickness of the plate. The crater depth for two different crater shapes is also defined in the figure.

and the penetrator may not match well with those observed in experiments when such tests are indeed performed. The results presented herein lead one to conclude that high kinetic energy ceramic rods can perforate metallic targets.

Target plate made of 4340 steel

For an impact speed of 0.5 km/s, the deformation patterns are similar to that for an aluminum target described above. Whereas initially the inner portion of the ceramic rod close to the axis of symmetry failed as was the case for an aluminum plate, subsequently the portion of the penetrator near the target–penetrator interface buckled because of the high resistance to penetration offered by the strong and dense steel plate. The failure of the rod material was due to the spall zone created at the axis of symmetry by tensile waves generated by the reflection of compressive waves from the free lateral surface of the rod. The rod material near the target–penetrator interface also expanded by sliding along the interface and buckled. The spall zone propagated to the upper part of the rod and its failure due to buckling also continued. Even though the plate bent, there was no noticeable crater formed.

The transition from axisymmetric buckling failure mode to mushrooming failure mode was observed for impact speeds of approximately 1 km/s. This deformation mode in which both the target and the penetrator material near the target–penetrator interface expand is less damaging for the penetrator, but more damaging for the target.

At the impact speed of 2 km/s, as shown in Fig. 4, the sequence of events is totally different from that at the impact speed of 0.5 km/s. Initially, the ceramic near the outer surface of the rod and close to the impacted end fails, making the penetrator nose somewhat pointed. There is a small crater formed

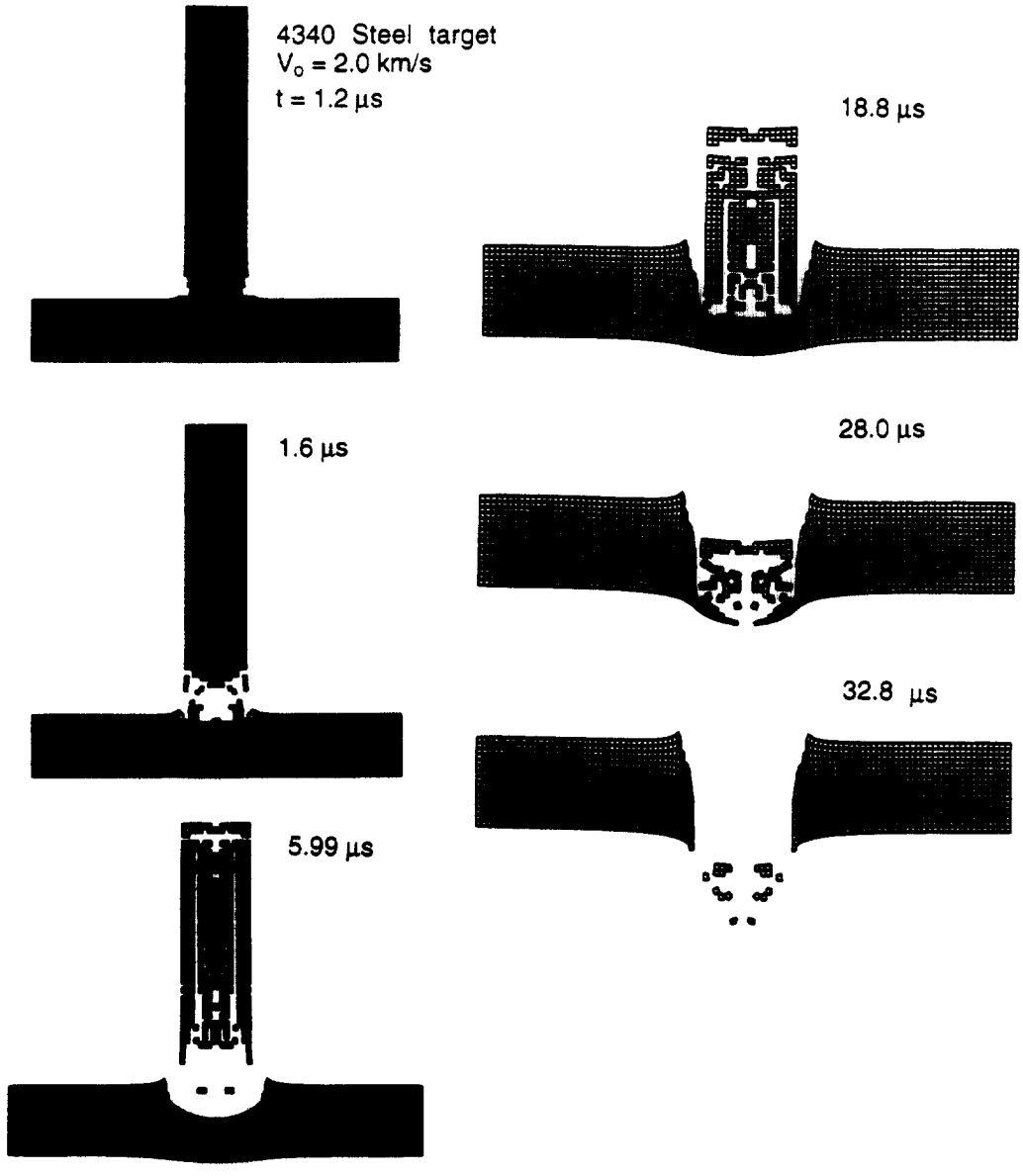

Fig. 4. Deformed configurations of the ceramic penetrator and the steel plate at different instants of time for an impact speed of 2 km/s.

in the steel plate at 1.6 μs and the ceramic material near the penetrator nose has been eroded giving rise to a gap between the penetrator and the target. Multiple impacts occur between the rod and the plate, the crater continues to enlarge, the plate is eventually perforated and essentially all of the penetrator is destroyed. The cylindrical surface of the crater is smooth even though the assumed value of the failure strain is relatively large.

For higher impact speeds, an impact flash is generated at the instant of impact, high-intensity stress waves propagate into the rod and the target and cratering of the plate surface and penetration of the rod commence immediately. Since, on initial impact, the peak pressure at the interface far exceeds the material strength of the rod and target, the penetrator front suffers hydrodynamic-like erosion, while the remainder of the rod enters the cavity undeformed. The crater deepens and its bottom expands due to the pressure exerted by the fluid-like expanding flow of the eroding rod nose. Intense shearing stresses are developed in the target material adjoining the target–penetrator interface. Plate failure occurs by one or more mechanisms described by Zukas[5].

At higher impact speeds the crater formed in the steel plate prior to complete perforation is hemi-toroidal rather than hemispherical and the penetrator nose shape becomes conical with a pointed nose and the cone angle of 45° immediately after impact. This change in the geometry of the rod makes the penetration process more efficient. For example, at

an impact speed of 3 km/s, the penetration depth increases from 0.8 mm at $t = 1.6\ \mu s$ to 6.4 mm at $t = 5.59\ \mu s$. A significant part of the rod is eroded away and its nose shape changes from conical to a concave cutter. Multiple impacts increase both the depth and the diameter of the crater which transforms from a hemi-toroidal shape to a bubble-type. The number of multiple impacts and the shape and length of the residual penetrator vary with the impact speed. Higher the impact speed, greater the length of the residual penetrator after completion of the perforation process. For impact speeds of 5 and 6 km/s typical patterns of penetrator-target interaction were observed to be as follows: sharpening of the penetrator nose to conical with the remainder of the penetrator virtually undamaged, breaking away of the conical portion leading to a flat nosed solid rod, secondary impact leading to erosion of the rod nose material near its axis of symmetry thus resulting in a cutter nose, multiple impacts damaging the rod, the crater shape changing from hemi-toroidal to parabolic and to bubble-type cavity.

Target plate made of a D17 tungsten alloy

Figure 5 depicts deformed configurations of the ceramic penetrator and the tungsten target plate at different times for impact speeds of 3, 3.5 and 4 km/s. Whereas the tungsten plate is not perforated at an impact speed of 3 km/s, complete perforation occurs at the other two speeds and the shape of the hole formed depends noticeably upon the impact speed. For impact speed of 3 km/s, the central part of the penetrator head experiences maximum shear deformations and rapid failure of the front part of the rod creates a new flat surface at $t = 2.5\ \mu s$. Reflected tensile waves from the free lateral surface cause failure at inner points of the rod. Multiple impacts between the rod and the plate transfer momentum and energy to the target. At $t = 11.2\ \mu s$, the tungsten at the crater surface behaves as a compressible fluid. The crater is nearly hemispherical and both maximum shear stresses and plastic strains occur at points on the crater surface. Subsequent impacts between the rod and the crater surface transform the hemispherical shape of the crater into a cylindrical one and the depth of the final crater formed exceeds the thickness of the plate. The crater and hence the hole formed is parabolic at impact speeds of 3 and 3.5 km/s, a cylindrical hole is formed at impact speeds of 4 km/s and higher. Also significant bulging out and distortions of the penetrator material occur and the hole diameter is much larger than the diameter of the ceramic rod. For an impact speed of 4 km/s, the crater depth just prior to perforation exceeds twice the initial thickness of the plate.

Deformed configurations of the ceramic rod and the tungsten plate for an impact speed of 5 km/s are shown in Fig. 6 wherein contours of effective plastic strain in the two bodies at $t = 1.6\ \mu s$ are also plotted. Significant compressive plastic strains occur in the penetrator near the penetrator–target interface. The embedding followed by mushrooming and failure of the rod nose creates plastic flow and a hemispherical cratering of the target. The immersed nose experiences strong compression and unloading waves reflected from the free lateral surfaces cause erosion of the penetrator material resulting in a shape with cutting outer edges. Intensive plastic flow at the crater surface expands downwards and creates a large hemispherical cavity. Secondary impacts cause the fluid-like plastically deforming tungsten material to flow along the crater surface. At $t = 14\ \mu s$, the bottom part of the plate is intensively thinning, stretching and bending due to inertial effects. At an impact speed of 6 km/s, the penetration and perforation mechanisms are essentially similar to those for an impact speed of 5 km/s, but more damage is caused to the tungsten plate. All of the ceramic rod is consumed at an impact speed of 6 km/s. However, the length of the ceramic rod that survives increases with an increase in the impact speed.

We have plotted in Fig. 7, the evolution of the crater depth for steel and tungsten plates struck at normal incidence by ceramic rods at different speeds. The minimum impact speed at which complete perforation of the plate occurs in the two cases is quite different as expected because of the differences in the densities and material properties of the two materials. In each case, the time required to perforate the plate decreases monotonically with an increase in the speed of the rod.

For comparison, we have also studied the penetration/perforation of a tungsten rod, identical in shape to the ceramic rod, into a tungsten plate. Figure 8 depicts the deformed configurations of the rod and the plate at different times for impact speeds of 0.5, 3 and 5 km/s. For an impact speed of 0.5 km/s, the tungsten rod undergoes significant mushrooming and lateral expansion, but no perforation occurs. At $V_0 = 2$ km/s, the tungsten rod survives mushrooming, embedding into the target and perforates a wide hole whose diameter equals nearly twice that of the rod. When the impact speed equals 3 km/s, the penetration process is similar to that found for the ceramic rod moving at 5 km/s. However, the length of the residual tungsten rod is much greater than that of the residual ceramic rod and the residual tungsten rod undergoes very little damage except near the front end. In addition, multiple impacts do not occur for a tungsten rod impacting a tungsten plate. At impact speeds of 5–6 km/s the time required for ceramic rods to perforate through tungsten plates is slightly less than that for geometrically identical tungsten rods. Thus, the penetration–perforation capability of a ceramic rod into a tungsten plate approaches that of a tungsten rod.

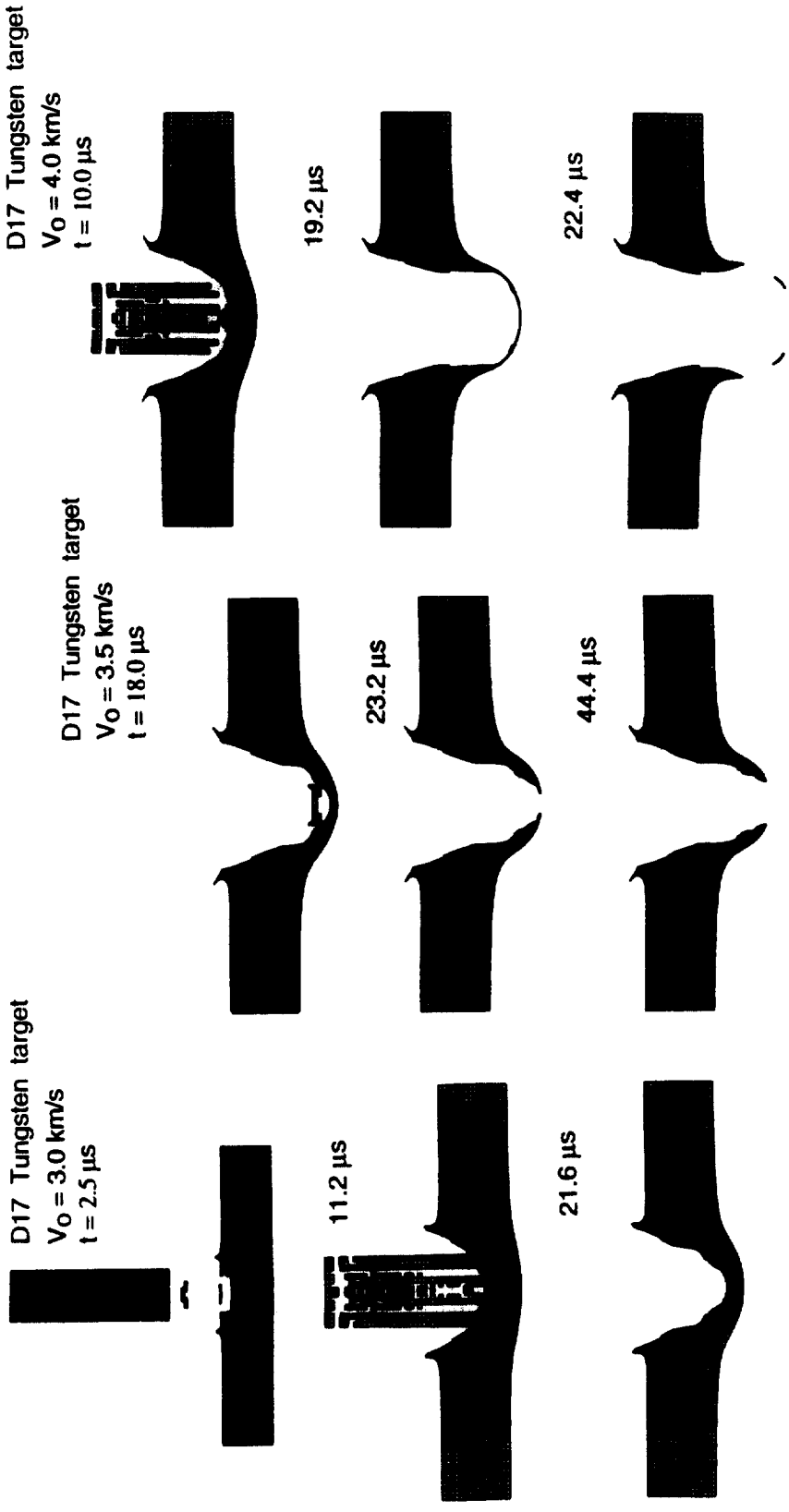

Fig. 5. Deformed configurations of the ceramic penetrator and the tungsten plate at different times and at impact speeds of 3, 3.5 and 4 km/s.

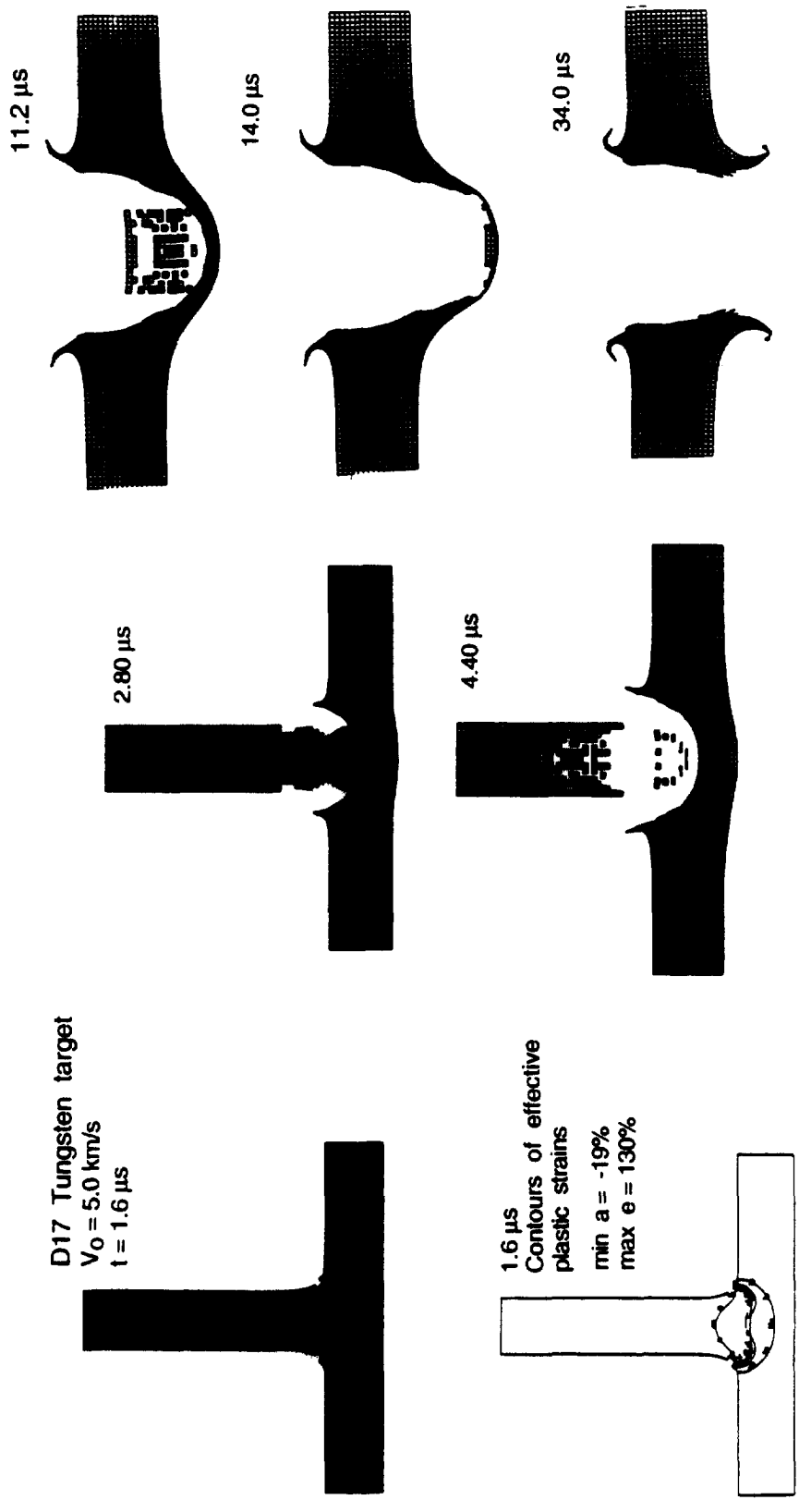

Fig. 6. Deformed configurations of the ceramic penetrator and the tungsten plate at different times and at an impact speed of 5 km/s.

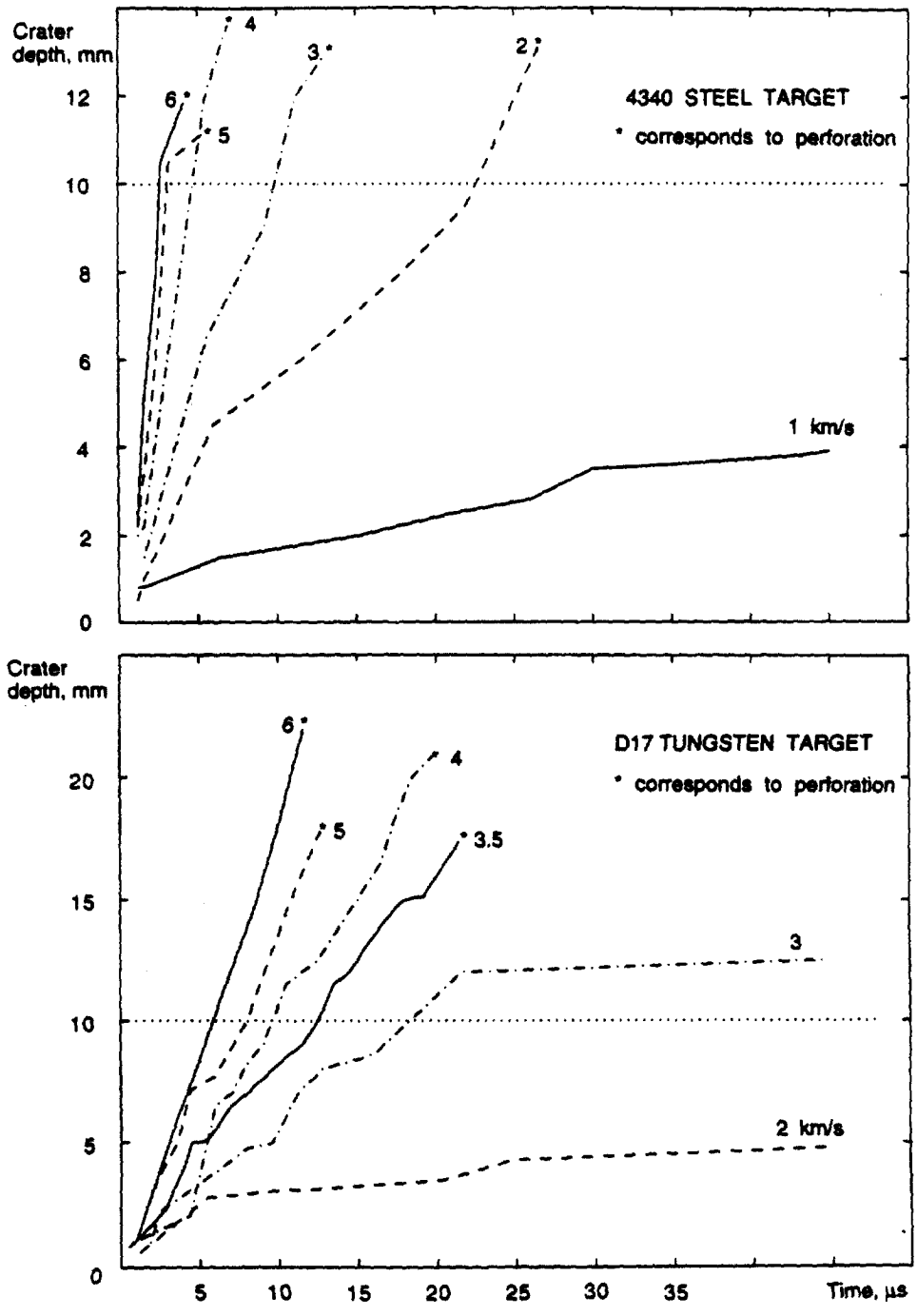

Fig. 7. Time histories of the evolution of crater depths in the 4340 steel and D17 tungsten plates struck at normal incidence by a ceramic rod at different impact speeds. The dotted line corresponds to the initial thickness of the plate.

For the problem being studied, the penetrator and the target support conditions are fixed. Thus, the crater depth and the residual penetrator speed when the target is perforated depend upon the mass density, yield strength, work-hardening and failure strain of the target material. As expected, higher mass density, yield strength and failure strain for the tungsten material result in lower values of the crater depth. Our numerical experiments with 'artificial' aluminum targets described above indicate that the mass density and the failure strain influence significantly the crater's shape and depth. Rosenberg and Dekel [12, 13] have also shown through numerical experiments that the failure strain affects noticeably the penetration depth and at high values of the penetrator length/penetrator diameter a low-

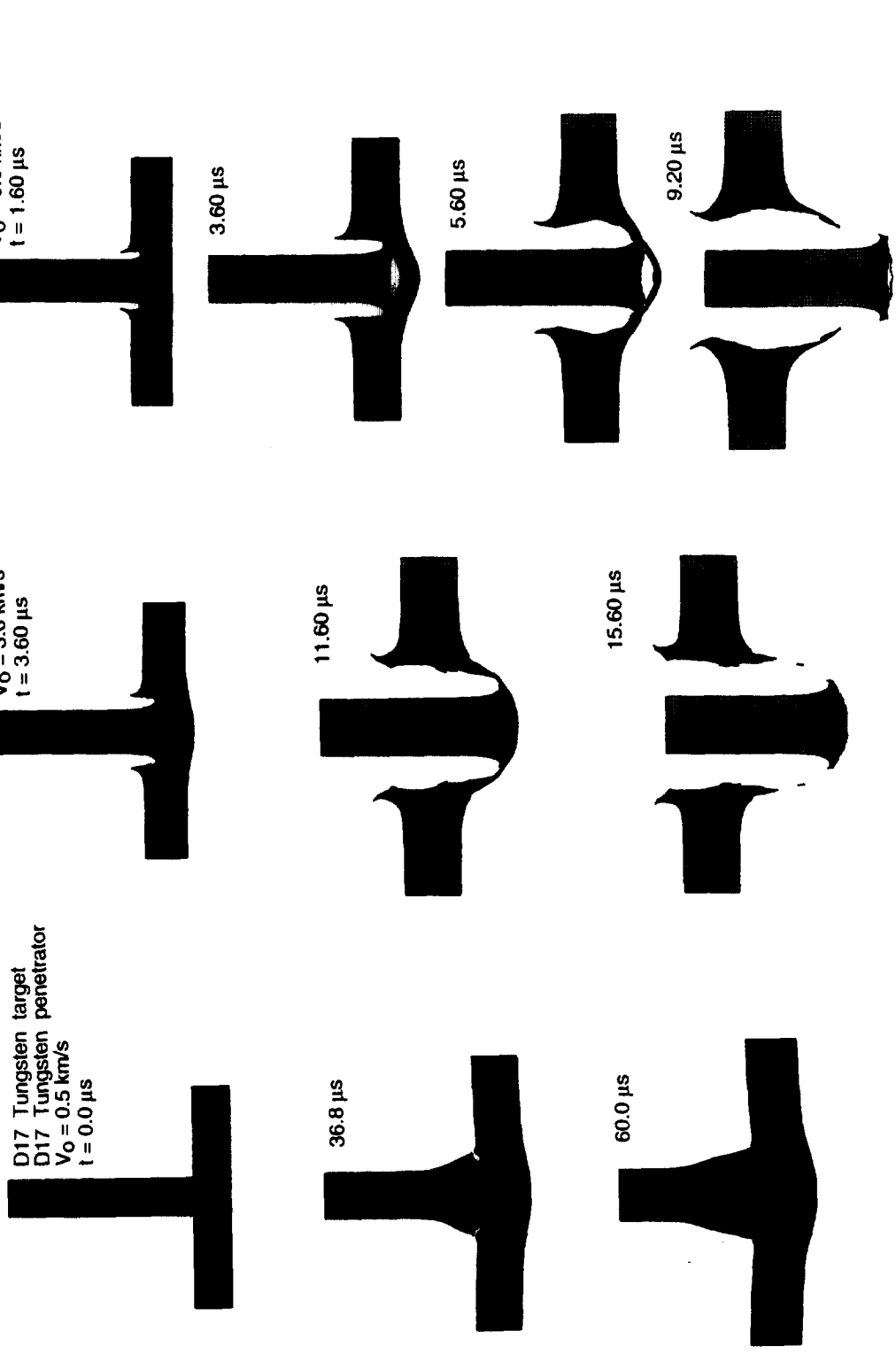

Fig. 8. Deformed configurations of the tungsten penetrator into a tungsten plate at different times for impact speeds of 0.5, 3 and 5 km/s.

strength projectile can be more efficient than a high-strength one. This suggests that a ceramic rod should be able to perforate a hard target as is confirmed by our simulations. We note that Littlefield *et al.* [14] used the eroding element concept to simulate the penetration of tungsten rods into steel targets and found a good agreement between computed penetration depths and those observed experimentally. Bless *et al.* [15, 16] have conducted penetration tests with ceramic rods, but the impact speeds used were too low to result in any significant crater formation. This is consistent with our numerical simulations. Apparently, they found it difficult to conduct reverse ballistic tests (a moving target hits a stationary rod) at high impact speeds.

Analytical penetration models include the one-dimensional models of Alekseevskii [17] and Tate [18] and the cavity expansion model of Forrestal *et al.* [19] Rosenberg and Dekel [12, 13] have shown that the one-dimensional models are not valid for simulating two-dimensional tests. Furthermore, these one-dimensional models assume a semi-infinite target and we have analyzed targets of finite thickness. Ravid *et al.* [20] and Batra and Chen [21], among others, have developed models to analyze the normal perforation of metallic plates by essentially rigid projectiles. The unknown parameters presumed in the kinematically admissible flow field are found by a minimization technique. Because of the rather rapid failure of the ceramic rod, these models are not applicable to the present problem.

CONCLUSIONS

We have studied the axisymmetric penetration of the ceramic rod into aluminum, steel and tungsten plates. The ceramic is modeled as an elastic–plastic material with different properties in compression and tension and a material point is assumed to fail when the hydrostatic pressure there is tensile and exceeds the spall strength of the material. The plate material is modeled as an isotropic elastic/plastic with linear strain hardening and a material point is assumed to fail when the effective plastic strain there attains a critical value. Failed elements are deleted from further analysis.

Plates made of aluminum, steel and tungsten were found to be perforated by the ceramic rod. However, deformations of the ceramic penetrator and the shape of the hole formed depended strongly upon the impact speed. For aluminum plates, the hole was found to be smooth cylindrical for small values of the failure strain and rough hemispherical for large values of the failure strain. For the steel and tungsten plates, the nose shape was initially deformed from flat to conical and the conical part failed giving rise to a smaller flat-nosed rod. Subsequently, the rod material near its axis of symmetry and the front end failed resulting in a cutter edge. Multiple impacts between the rod and the crater formed in the plate eventually perforated the plate. The residual length of the rod after perforation was found to be more at higher impact speeds.

Acknowledgements—This work was supported by the U.S. Army Research Office grant DAAH04-95-1-0042 to the Virginia Polytechnic Institute and State University. We are indebted to Mr Forrest Flocker, a graduate student at the University of Missouri-Rolla and Miss Sharon Smale, an undergraduate student at VPI&SU, for help with DYNA2D and some of the computations. Miss Smale was supported by a grant from the NSF to VPI&SU.

REFERENCES

1. Brandon, D. G., Yeshurun, Y., Rosenberg, Z. and Ozeri, Y., Micromechanisms of impact failure in engineering ceramics. *Macro- and Micro-Mechanics of High Velocity Deformation and Fracture*. IUTAM Symposium on MMMHVDF, Tokyo, Japan, 1987, pp. 127–133.
2. Anderson, C. E. Jr, O'Donoghue, P. E., Lankford, J. and Walker, J. D. Numerical simulation of SHPB experiments for the dynamic compressive strength and failure of ceramics. *International Journal of Fracture*, 1992, **55**, 193–208.
3. Rosenberg, Z., Yaziv, D. and Bless, S. J., The shear strength of shock-loaded alumina as determined with embedded longitudinal and transverse manganin gauges. Report UDR-TR-86-123, University of Dayton Research Institute—Impact Physics Laboratory, 1989.
4. Bless, S. J., Impact behavior of ceramics. In *Dynamic Constitutive/Failure Models*, ed. A. M. Rajendran and T. Nicholas. Report AFWAL-TR-4229, Wright-Patterson Air Force Base, OH, 1988.
5. Zukas, J. A., *High velocity impact dynamics*. Wiley, New York, 1990.
6. Truesdell, C. A. and Noll, W. The nonlinear field theories of mechanics. *Handbuch der Physik*, Vol. III/3, ed. S. Flügge. Springer, Berlin, 1965.
7. Rajendran, A. M. Modeling the impact behavior of AD85 ceramic under multiaxial loading. *International Journal of Impact Engineering*, 1994, **15**, 749–768.
8. Rosenberg, Z. Dynamic uniaxial stress experiments on alumina with in-material manganin gauges. *Journal of Applied Physics*, 1985, **57**, 5087.
9. Whirley, R. G., Englemann, B. E. and Hallquist, J. O. *DYNA2D. A Nonlinear, Explicit Two-dimensional Finite Element Code for Solid Mechanics. User Manual*. Lawrence Livermore National Laboratory Report, UCRL-MA-110630, 1992.
10. Stetcher, F. P. and Johnson, G. R. Lagrangian computations for projectile penetration into thick plates. In *Computers in Engineering*, Vol. 2, ed. W. A. Grover, ASME, pp. 292–299, 1984.
11. Kimsey, K. D. and Zukas, J. A. Contact surface erosion for hypervelocity problems, BRL-MR-3495, 1986.
12. Rosenberg, Z. and Dekel, E. A computational study of the relation between material properties of long rod penetrators and their ballistic performance, unpublished.
13. Rosenberg, Z. and Dekel, E. A computational study of the influence of projectile strength on the performance of long-rod penetrators. *International Journal of Impact Engineering*, 1996, **6**, 671–677.
14. Littlefield, D. L., Anderson, C. E. Jr, Partom, Y. and Bless, S. J. The penetration of steel targets finite in

radial extent. *International Journal of Impact Engineering*, 1997, **19,** 49–62.

15. Brar, N. S., Bless, S. J. and Rosenberg, Z. Brittle failure of ceramic rods under dynamic compression. *Journal de Physique C*, 1988, **3,** 607–612.
16. Bless, S. J., Brar, N. S. and Rosenberg, Z., Failure of ceramic and glass rods under dynamic compression. In *Shock Compression of Condensed Matter*, ed. S. C. Schmidt, J. N. Johnson and L. W. Davison, Elsevier, Oxford, pp. 939–942, 1990.
17. Alekseevskii, V. P. Penetration of a rod into target at high velocity. *Combustion, Explosions and Shock Waves*, 1966, **2,** 63.
18. Tate, A. Further results in the theory of long rod penetration. *Journal of the Mechanics and Physics of Solids*, 1969, **17,** 141.
19. Forrestal, M. J., Okajima, K. and Luk, V. K. Penetration of 6061-T651 aluminum targets with rigid long rods. *Journal of Applied Mechanics*, 1988, **55,** 755–760.
20. Ravid, M., Bodner, S. R. and Holcman, I. Analysis of very high speed impact. *International Journal of Engineering Science*, 1987, **25,** 473–482.
21. Batra, R. C. and Chen, X. An approximate analysis of steady state axisymmetric deformations of viscoplastic targets. *International Journal of Engineering Science*, 1990, **28,** 1347–1358.